

SHOCKING CLOUDS IN THE CYGNUS LOOP¹

N. A. LEVENSON

Department of Physics and Astronomy, Bloomberg Center, Johns Hopkins University, Baltimore, MD 21218
levenson@pha.jhu.edu

AND

JAMES R. GRAHAM

Department of Astronomy, University of California, Berkeley, CA 94720
jrg@astron.berkeley.edu

To appear in The Astrophysical Journal, October 10, 2001

ABSTRACT

With *Hubble Space Telescope* Wide-Field Planetary Camera 2 observations of the Cygnus Loop supernova remnant, we examine the interaction of an interstellar cloud with the blast wave on physical scales of 10^{15} cm. The shock front is distorted, revealing both edge-on and face-on views of filaments and diffuse emission, similar to those observed on larger scales at lower resolution. We identify individual shocks in the cloud of density $n \approx 15 \text{ cm}^{-3}$ having velocity $v_s \approx 170 \text{ km s}^{-1}$. We also find the morphologically unusual diffuse Balmer-dominated emission of faster shocks in a lower-density region. The obstacle diffracts these shocks, so they propagate at oblique angles with respect to the primary blast wave. The intricate network of diffuse and filamentary H α emission arises during the early stage of interaction between the cloud and blast wave, demonstrating that complex shock propagation and emission morphology occur before the onset of instabilities that destroy clouds completely.

Subject headings: ISM: individual(Cygnus Loop) — shock waves — supernova remnants

1. THE SOUTHEAST KNOT OF THE CYGNUS LOOP

Supernova remnants and the interstellar medium act upon each other reciprocally. The energy of supernova remnants (SNRs) heats and ionizes the interstellar medium (ISM), and their blast waves govern mass exchange between the hot, warm, and cool phases of the ISM. In turn, the extant ISM determines the evolution of SNR blast waves as they propagate through the environment it provides. Thus, in order to understand the large-scale structure of the ISM, we must also discern the nature of shock evolution in inhomogeneous media.

The Cygnus Loop supernova remnant provides an ideal laboratory in which to examine these issues. It is relatively unobscured, with $E(B - V) = 0.08$ (Parker 1967), and nearby (440_{-100}^{+130} pc; Blair et al. 1999), so $1''$ corresponds to 7×10^{15} cm. It is a middle-aged supernova remnant, not only in terms of absolute lifetime, $\tau = 8000$ yr (Levenson et al. 1998, scaling for the revised distance), but more importantly because the interaction of the blast wave with the ISM dominates its evolution and its appearance at all wavelengths. At optical wavelengths, the outstanding features are due to decelerated shocks that propagate through dense interstellar clouds. Shocks that are reflected off the cloud surfaces propagate back through previously shocked material, further heating and compressing it, enhancing X-ray emission (Hester & Cox 1986).

One example of this characteristic interaction is the southeast knot. Fesen, Kwitter, & Downes (1992) drew attention to this apparently insignificant feature in the optical and X-ray emission, which has a small angular extent compared to the diameter of the Cygnus Loop. In

contrast to the SNR as a whole, the optical appearance of the southeast knot suggests that it represents only a very minor enhancement in the local ISM, or that the interaction is very young. Fesen et al. (1992) support the former interpretation, proposing that this represents the late stage of interaction with a small cloud that has been completely engulfed by the blast wave and is in the process of being shredded by fluid instabilities (Klein, McKee, & Colella 1994). X-ray imaging contradicts this interpretation, however, because the knot is located at the apex of a large-scale (0.5 degree) indentation in the eastern limb as traced by very low surface brightness X-ray emission (Graham et al. 1995; Levenson, Graham, & Snowden 1999). Thus, the obstacle is certainly large, extending at least 5 pc along the line of sight, and the interaction is at an early stage.

The optical emission is confined to a $2' \times 4'$ region, but the apparent insignificance of the southeast knot may belie its importance. The highest surface brightest optical and X-ray emitting regions of the Cygnus Loop are associated with the well-developed reflected and transmitted shocks that form in mature cloud–blast-wave interactions (e.g., Hester, Raymond, & Blair 1994). The morphology of these bright regions is notoriously complex because multiple shocks are present along the same line of sight. Only in a few cases is the geometry unambiguous, such as the western limb (Levenson et al. 1996). In addition, the development of fluid dynamic instabilities into the non-linear regime during the late phase of interaction adds to the challenge of interpreting the more prominent regions. These difficulties suggest that focussing on very recent interactions, although intrinsically fainter, may provide use-

¹ Based on observations with the NASA/ESA *Hubble Space Telescope*, which is operated by the Association of Universities for Research in Astronomy, Inc., under NASA contract NAS 5-2655.

ful insights into the sizes, shapes, and density contrasts characterizing the clouds in the vicinity of the Cygnus Loop.

In this work, we use the the *Hubble Space Telescope* (*HST*) to examine the variation in optical line emission on scales of $0''.1 \equiv 7 \times 10^{14}$ cm, assuming a distance of 440 pc. Clarifying the geometry of the emitting regions, we trace the motion of the blast wave in this cloud interaction and quantify the relevant physical processes. We present the data in §2, discuss the morphology and physics in §§3 and 4, respectively, and summarize our conclusions in §5.

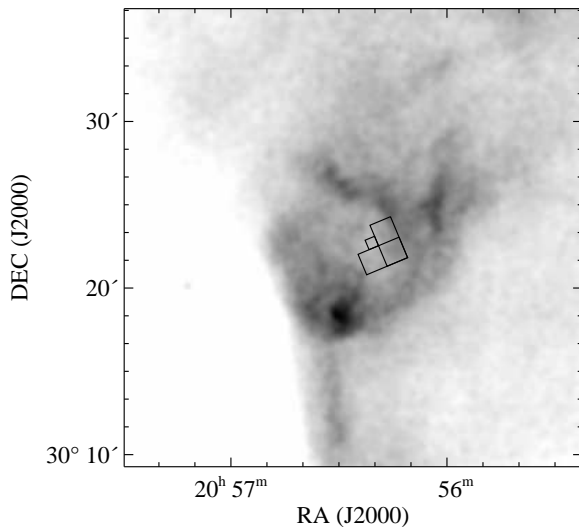


FIG. 1.— WFPC2 field of view overlaid on soft X-ray image of the surrounding field. The bright optical emission is not coincident with the associated X-ray enhancement.

2. OBSERVATIONS AND DATA REDUCTION

We obtained the data from the *HST* archive at the Space Telescope Science Institute. The observations with the Wide-Field Planetary Camera 2 (WFPC2) were performed 1994 November 25 for Program 5774 (Principal Investigator J. Hester). Figure 1 illustrates the location and orientation of these observations on the soft X-ray image of the surrounding field obtained with the *ROSAT* High Resolution Imager (Graham et al. 1995). A total exposure of 2200 s in two frames (to facilitate removal of cosmic rays) was taken through each of three narrow filters. The F502N filter includes [O III] $\lambda 5007$, F656N includes $H\alpha$, and F673N includes [S II] $\lambda\lambda 6717 + 6731$. We employed standard *HST* pipeline processing, then used the IRAF² task `crrej` to remove cosmic rays in the average images. We assembled the individual detector images into a single mosaic using IRAF’s `wmosaic`. Figure 2 contains the $H\alpha$ image, with the detectors PC1, WF2, WF3, and WF4 identified counterclockwise, beginning at the upper left. The $0''.046$ pixels of the PC1 correspond to 3×10^{14} cm, and the $0''.1$ WF pixels are equivalent to 7×10^{14} cm. We apply the flux calibration of Holtzman et al. (1995), using the 1998 calibration. The system throughput is 0.104, 0.111, and 0.052 for $H\alpha$, [S II], and [O III], respectively

(*HST* Data Handbook 1998).

3. MORPHOLOGY

The supernova blast wave moves from west to east across the field of view and has recently encountered a cloud of denser-than-average interstellar gas. In the *HST* field, we observe the southern section of the interaction, which extends out of the field of view to the north for another $4'$. We combine the three narrow-band data sets in a false-color image (Figure 3), with $H\alpha$ mapped in red, [S II] in green, and [O III] in blue. Magenta thus corresponds to strong $H\alpha$ and [O III], while yellow shows where $H\alpha$ and [S II] appear together. Cyan, which would come from strong coincident [O III] and [S II] is almost entirely absent from the image.

In Figure 3, color and morphology are strongly correlated. The shock morphology is distinctly stratified, with several characteristic types of filaments dominating the composition of the image. Similar to larger-scale observations of the Cygnus Loop at lower resolution, the two fundamental characteristic morphologies—sharp filaments and diffuse emission—correspond to two distinct viewing geometries (Hester 1987). The sharp filaments arise in wavy sheets viewed edge-on, through tangencies, and in general these shocks propagate in the plane of the sky. This is the most favorable geometry for unambiguously viewing the stratification of the post-shock flow as it cools and recombines. The images therefore reveal in turn the Balmer-dominated and [O III]-dominated regions behind the shock front. In contrast, shocks viewed face-on produce diffuse emission. Because larger swept-up column densities are required for this diffuse emission to be detectable, it is more likely to exhibit the characteristics of a complete radiative shock, namely strong [S II] emission relative to [O III] and $H\alpha$.

Toward the north and west the morphology becomes less filamentary, and secondary colors (magenta and yellow), as opposed to primary colors, become more common, with the superposition of multiple cooling stages observed along the line of sight. Green and yellow are prevalent in the western sections of the southern filaments. This is most apparent at the heel of the emission, which delimits the western extent of the cloud in WF3, the lower right quadrant of the image. The bright yellow complex at this location traces strong $H\alpha$ and [S II], which is characteristic of shocks that have swept up a substantial column ($N_H \gtrsim 10^{18} \text{ cm}^{-2}$) and formed complete cooling and recombination zones.

The slowest shocks show up as [S II] (green) only; occasionally these regions appear as high surface brightness knots (e.g., at the bottom edge of WF2, the lower left quadrant). In these instances, the primary blast wave is strongly decelerated in the dense cloud medium. More common is the extended, faint [S II] emission, which is widespread across WF2 and WF3. In general, this relatively smooth [S II] emission occurs by itself, unassociated with $H\alpha$ or other filaments. This low surface brightness [S II] emission is bounded on the western side by a sharp edge that delineates the current location of the shock within the cloud. This edge can be traced from the

² IRAF is distributed by the National Optical Astronomy Observatories, operated by the Association of Universities for Research in Astronomy, Inc., under cooperative agreement with the National Science Foundation.

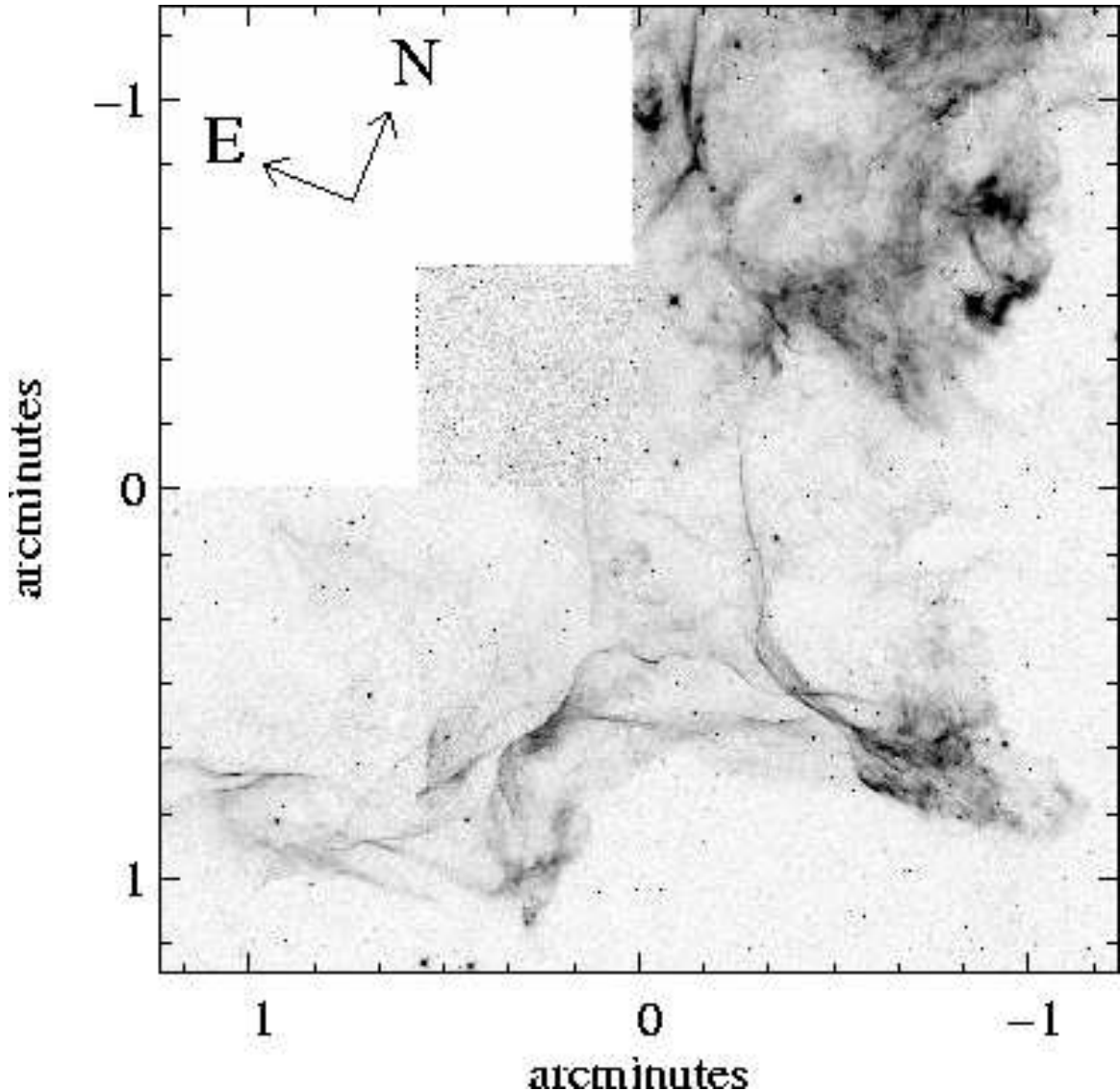


FIG. 2.— Southeast knot in the light of $H\alpha$. The image is scaled linearly from 0 (white) to $4 \times 10^{-14} \text{ erg cm}^{-2} \text{ s}^{-1} \text{ pixel}^{-1}$ (black). Shocks viewed face-on produce diffuse emission, while sharp filaments are characteristic of edge-on shocks. The upper left quadrant contains the smaller PC1 detector, with WF2 at the lower left, WF3 at the lower right, and WF4 at the upper right.

bright green knots at the western limit of WF2, then running north and northwest into WF3, around the bright heel and to the northeast up into the bright complex in WF4 at the upper right. This edge probably represents the original and undisturbed surface of the cloud, since the interaction is recent and has not yet had a significant dynamical effect on the cloud. In several locations, we identify the initial development of the radiative zone, finding [S II] emission downstream of $H\alpha$ filaments (near the right center of WF2 and at the bottom of the heel in WF3, for example). The [S II] emission is typically offset behind the shock front by $0''.5$ ($3 \times 10^{15} \text{ cm}$). Unlike the sharply-peaked $H\alpha$ filaments, the [S II]-emitting region is resolved, with flux extending over an arcsecond-scale region of the sky behind any distinct portion of the shock front.

The brightest incomplete [O III] filaments and the [S II]-emitting shocks in the heel region are clearly physically associated. At the center of the field of view the two

main $H\alpha$ /[O III] filaments are part of a segment of blast wave that is propagating to the southeast. Two tangencies to this surface form the two most prominent incomplete [O III] shocks and their preceding Balmer filaments. The filament turns through 45 degrees to form a funnel-like cusp with the heel. Tracing the upper filament towards the heel, the [O III] emission first merges with the $H\alpha$, producing magenta in the false-color image. It then disappears as it eventually joins the shocks driven into the western extremities of the cloud. Similar morphologies are formed by the blast-wave-cloud collision farther north in the XA region (Hester & Cox 1986).

Emission from shocks with well-developed cooling and recombination zones comprise the northern section of the interaction and fill the WF4 field. The absence of large-scale filamentary structures implies that these shocks are more nearly face-on and are lighting up the surface of the cloud. The sharp filamentary structures in this region have [O III] emission, appearing blue and magenta, and

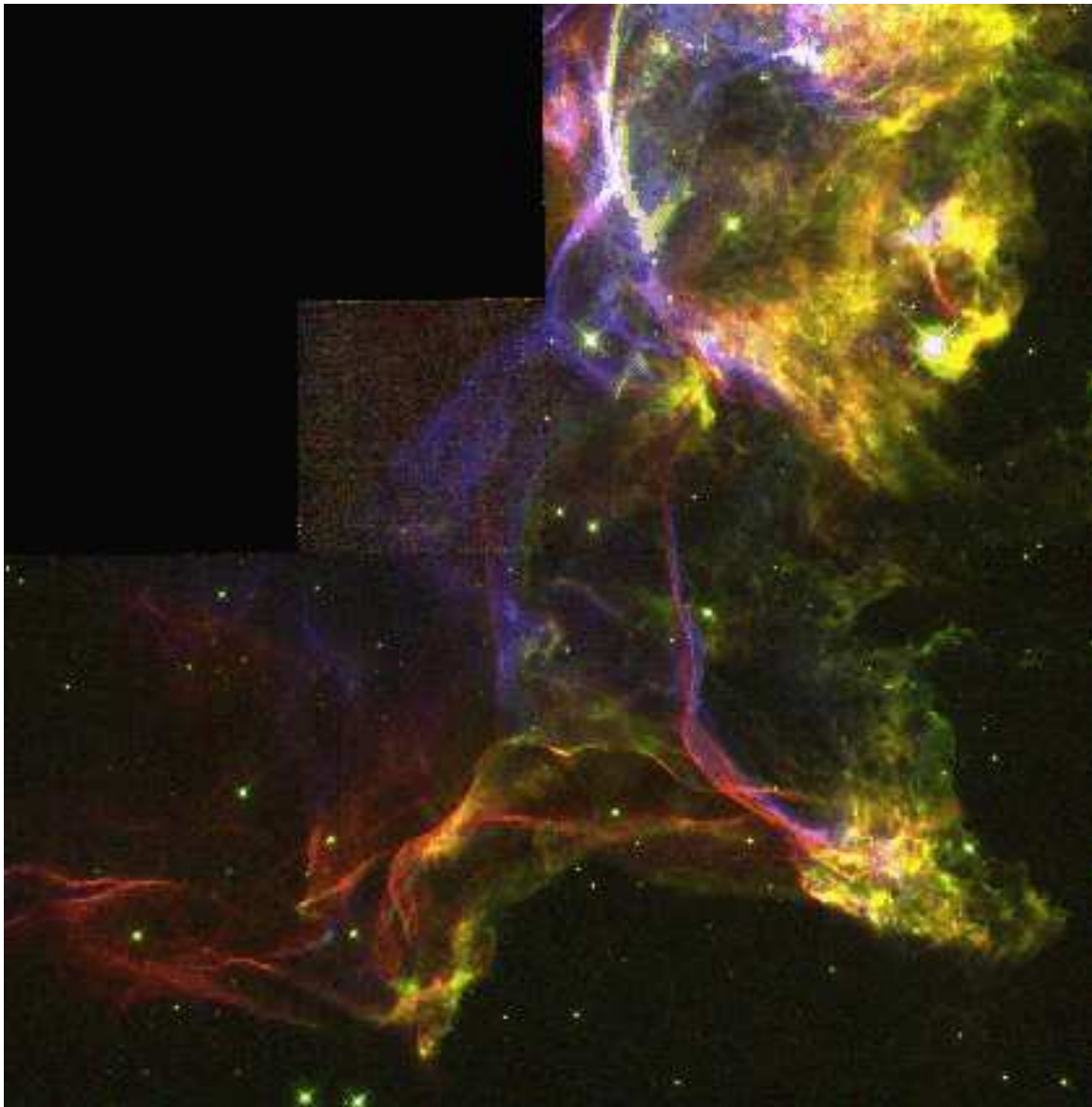


FIG. 3.— False-color image of the southeast knot. $H\alpha$ emission is mapped in red, [S II] in green, and [O III] in blue. The complete radiative cooling zone has developed in bright yellow regions, with strong $H\alpha$ and [S II]. The bright “heel” at the lower right of the image marks the distinct cloud edge. Pure red filaments occur at non-radiative shock fronts. In the examples that have swept up sufficient column density, [O III] emission appears close behind, or is dominant, without obvious associated $H\alpha$ filaments, in regions of incomplete cooling.

can be connected to the Balmer-dominated and incomplete shocks farther south. These less-decelerated shocks appear in projection against this northern field, so the relative east-west position does not correspond to absolute advancement within the cloud.

The prominent, sharp-edged, red structures are Balmer-dominated filaments and appear as a part of a continuous, gently rippled sheet, as in the extreme southern section of WF2. These filaments are due to fast shocks ($v_s > 100 \text{ km s}^{-1}$) that excite $H\alpha$ emission by electron collisions in pre-shock gas that is predominantly neutral and atomic (Chevalier & Raymond 1978; Chevalier, Raymond, & Kirshner 1980). The excitation is confined to in a narrow zone immediately behind the shock front, and the resultant face-on $H\alpha$ surface brightness is low. Thus, in these “non-radiative” shocks, the filaments are seen as bright, sharp structures when the shock front is close to

tangency with the line of sight (cf. Hester 1987). Since the gas must be neutral to produce these filaments, they also mark regions where the gas is being shocked for the first time, delineating the outer boundary of the blast wave. Gas-dynamic phenomena in which the gas is multiply shocked, including reflected shocks, cannot produce Balmer-dominated filaments.

The Balmer filaments with no associated [O III] (blue) emission have swept up $N_H < 10^{17} \text{ cm}^{-2}$. These shocks has suffered the smallest deceleration. While the general trend in this image is for shocks to propagate from west (left) to east (right), filaments at skewed angles reveal their direction of propagation when they have swept up sufficient column for [O III] ($N_H \gtrsim 10^{17} \text{ cm}^{-2}$) or [S II] ($N_H \gtrsim 10^{18} \text{ cm}^{-2}$) emission to be detectable downstream.

At the center of the field are two good examples of patches of [O III] emission that are correlated with Balmer-

line filaments. Their appearance is consistent with a volume of [O III] emission bounded on the upstream side by the Balmer-line-delimited shock transition. The shock at this location is propagating to the southeast. Farther east in the PC1 is an amorphous region of pure [O III]. Any associated $H\alpha$ is very faint, suggesting that the direction of propagation of the blast wave here is more nearly face-on. The [O III]-dominated incomplete shocks extend to the top of the image and are interspersed with and project against more complex and diverse emission morphologies.

4. NON-RADIATIVE FILAMENTS AND INCOMPLETE SHOCKS

In these images, the relationship between the Balmer filaments and the downstream [O III] emission of the incomplete shock distinguishes the physical conditions that are present. We examine the filament near the center of the WF3 field, which provides a particularly clear example. At this location, a Balmer-line filament bounds an incomplete cooling and recombination zone. The ratio of [O III] to $H\alpha$ surface brightness reaches a plateau of about 6 at a distance 5×10^{15} cm behind the current location of the shock front, which the center of the $H\alpha$ emission defines. This value exceeds the maximum of about 2 that can occur in fully radiative shocks, identifying it unambiguously as an incomplete shock.

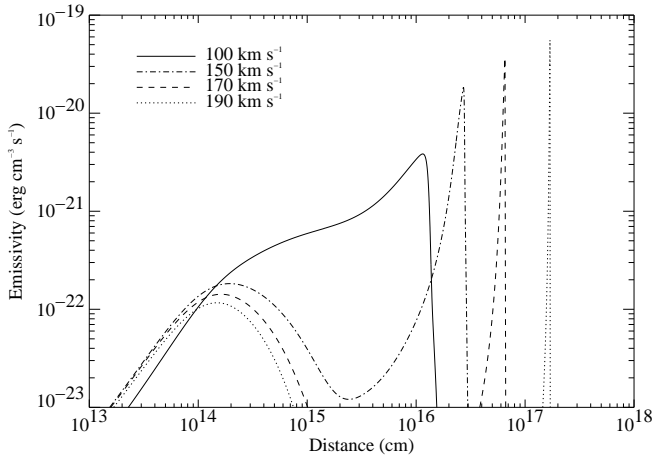


FIG. 4.— Model [O III] line emissivity as a function of distance behind shock front for various shock velocities and $n = 1 \text{ cm}^{-3}$. While in the $v_s = 100 \text{ km s}^{-1}$ case, the profile rises gradually and reaches a maximum 10^{16} cm behind the shock front, in the faster examples, the brightest emission is sharply peaked farther behind the shock.

The key parameter that determines the location and width of the [O III] emission zone is swept-up column density behind the shock front. More exactly, the [O III] surface brightness profile constrains the ambient density and shock velocity. In general, [O III] emission rises gradually and closer to slower shock fronts, while the profile is sharply peaked and offset farther downstream from fast shocks, as Figure 4 illustrates. The effect of increasing density is to shift the primary [O III] peak closer to the shock front. (In all cases, the initial, smaller peak about 10^{14} cm behind the shock front occurs while oxygen is excited to higher ionization states, when [O III] is not the dominant coolant.)

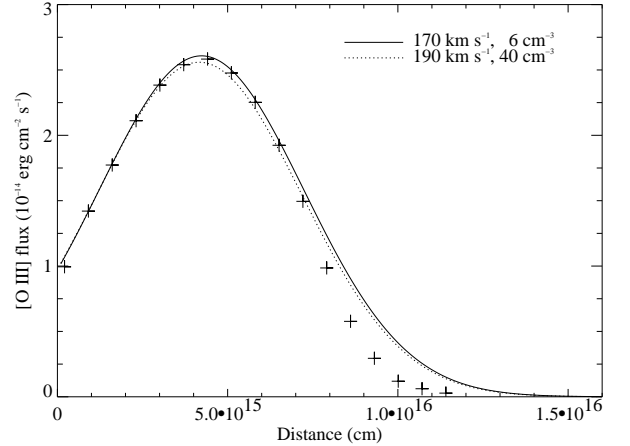


FIG. 5.— Observed and model [O III] emission profiles. We find good agreement between the data (*crosses*) and model profiles having $v_s = 170$ (*solid line*) to 190 (*dotted line*) km s^{-1} , assuming line of sight depths of 9×10^{17} and 1×10^{18} cm, respectively.

We apply updated versions of the models described by Raymond (1979) and Cox & Raymond (1985) for shock velocities ranging from 100 to 190 km s^{-1} , convolving these models with the instrumental profile measured from point sources in the field of view. The Balmer filament fixes the location of the shock transition, and the free parameters are shock velocity, pre-shock density, and depth of the surface along the line of sight. While the models include magnetic fields, in the hot, post-shock gas these data trace, thermal pressure dominates, and the effect of magnetic pressure is negligible. We find good agreement with both $v_s = 170$ and 190 km s^{-1} , with density $n = 15$ and 40 cm^{-3} respectively, in these two cases (Figure 5). We cannot significantly distinguish between these fast shocks because the instrumental resolution dominates the emission profile, but we prefer $v_s = 170 \text{ km s}^{-1}$ because the location of peak emission of this model better matches the observations. The residuals between the model and data at distances around 10^{16} cm are likely the result of poor subtraction of the local background where the flux is extremely low. Thus, we adopt the model parameters $v_s = 170 \text{ km s}^{-1}$ and $n = 15 \text{ cm}^{-3}$. In calculating the total flux, we initially assume that the geometry of the emission region is a thin sheet that extends 3×10^{17} cm in the line of sight, which is the observed extent of the filament across the image. Comparison of the observed and predicted intensities implies that the line of sight depth of the filament is in fact factors of 3 to 4 times its extent in the plane of the sky. This is a natural result because our selection bias favors bright filaments, which tend to be those with the greatest extent along the line of sight. The inferred velocity is robust against uncertainties in the assumed distance to the Cygnus Loop, while the derived densities are inversely proportional to distance.

For comparison, we compute the pressure from the X-ray observations of the same region. The surface brightness measured with the *ROSAT* High Resolution Imager corresponds to an emission measure of $70 \text{ cm}^{-5} \text{ pc}$. Here we assume a temperature $T = 2 \times 10^6 \text{ K}$ and solar abundances with two caveats: the temperature in this small region may be somewhat different than the average temperature, which is weighted by the brightest X-ray emis-

sion; and gas-phase depletion and subsequent grain destruction may alter the abundances (Vancura et al. 1994). Using the line of sight depth 10^{18} cm determined above and a 20% contribution of metals to the electron density, n_e , we require $n_e = 16 \text{ cm}^{-3}$. Thus, pressure $P = 8.7 \times 10^{-9} \text{ dyne cm}^{-2}$, which is comparable to the ram pressure that drives the cloud shock, based on the best-fitting parameters above.

These Balmer filaments and their associated incomplete shocks are distinct from those observed around the perimeter of the Cygnus Loop. In those cases, the filaments define the nearly-circular undisturbed blast wave and are continuous over scales of $40'$ (Levenson et al. 1998). The corresponding shocks propagate through a much less dense medium than the southeast cloud provides. Sankrit et al. (2000), for example, find $n = 2-4 \text{ cm}^{-3}$ and $v_s \sim 170 \text{ km s}^{-1}$ in a filament on the northeast periphery, based on ultraviolet line fluxes and intensity ratios. Assuming the same initial blast wave properties at the northeast limb and in the southeast knot, we conclude that the latter must be a younger interaction.

The overpressure that has developed behind the southeast shock drives it strongly into the cloud at a pressure exceeding that of the primary blast wave, as measured in other cloud encounters of the Cygnus Loop (Raymond et al. 1988; Hester, Raymond, & Blair 1994). The maximum overpressure of a cloud interaction is a factor of 3 once steady flow is established (McKee & Cowie 1975), or up to a factor of 6 when the blast wave encounters a plane of material (Spitzer 1982), which is more similar to this very early stage of interaction with a large cloud. The greater overpressure of the southeast knot is indicated not only in comparison with the northeastern filament, but also (and more significantly) when the average blast wave pressure, $P_{BW} \approx 5 \times 10^{-10} \text{ dyne cm}^{-2}$, derived from global X-ray data (Ku et al. 1984) is considered. The large overpressure at the southeast knot therefore indicates highly non-steady flow. A shock having $v_s = 170 \text{ km s}^{-1}$ is unstable unless the transverse magnetic field $B \gtrsim 10 \mu\text{G}$, but because the timescale for the development of secondary shocks is long (on the order of 10^4 years), they do not appear yet in this case (Innes 1992). Thus, the transient nature of the current conditions is expected. Only later will a slower, large-scale, coherent shock arise in a more developed interaction, similar to the western edge of the Cygnus Loop, for example.

Multiple shocks along the line of sight confuse the [O III] profile in several other locations where Balmer emission bounds a region of bright [O III], so we cannot directly

compare with the models, but we can characterize them qualitatively. We identify the Balmer filament at the center of the mosaicked field as a region of lower density, because the [O III] emission is broader and offset farther downstream. Immediately behind the filament at the west-center of the WF2 field, the fully-radiative signature of [S II] implies that this is a higher density region. The emission at the extreme southeast of the WF2 field consists exclusively of $\text{H}\alpha$, which suggests that the shock propagates through lower density here, perhaps in the extended envelope of the cloud. Furthermore, this region includes not only the sharp filaments that characterize the edge-on view, but also more diffuse emission where the shock surface is viewed at oblique angles. Thus, this region must be *intrinsically* bright. The emissivity depends linearly on v_s and n (Raymond 1991), so the shock velocity is higher here.

5. CONCLUSIONS

The *HST* images of the interaction between the Cygnus Loop blast wave and an interstellar cloud reveal emission variations on the smallest measurable scales (3×10^{14} cm). The blast wave cannot be identified as a single, uniform entity, but is broken into a complex of interacting shock fronts as it encounters the obstacle. We identify the characteristic morphology of sharp filaments, where a shock front is viewed edge-on, and diffuse emission, where the view is face-on, on the sub-arcsecond scales that WFPC2 probes. The [O III] profile immediately behind the shock front that Balmer-dominated filaments define reveals relatively fast shocks ($v_s \approx 170 \text{ km s}^{-1}$) in the high-density ($n \approx 15 \text{ cm}^{-3}$) cloud medium. Balmer filaments without associated [O III] or [S II] emission arise in slightly lower-density regions behind faster shocks. Because this emission is intrinsically bright, we detect the diffuse component, which is viewed obliquely, as well as the more common sharp filaments where the shock front is viewed edge-on. Exhibiting extensive networks of non-radiative shocks, the southeast knot must represent the early stage of interaction between the cloud and blast wave. This example thus illustrates that complex shock propagation and emission morphology occur before the onset of instabilities that destroy clouds completely.

We thank Ravi Sankrit for computing the shock model emission profiles. Support for this work was provided by NASA through grant number AR-08005 from the Space Telescope Science Institute, which is operated by AURA, Inc., under NASA contract NAS 5-26555.

REFERENCES

- Blair, W. P., Sankrit, R., Raymond, J. C., & Long, K. S. 1999, *AJ*, 118, 942
 Chevalier, R. A., & Raymond, J. C. 1978, *ApJ*, 225, L27
 Chevalier, R. A., Raymond, J. C., & Kirshner, R. P. 1980, *ApJ*, 235, 186
 Cox, D. P., & Raymond, J. C. 1985, *ApJ*, 298, 651
 Fesen, R. A., Kwitter, K. B., & Downes, R. A. 1992, *AJ*, 104, 719
 Graham, J. R., Levenson, N. A., Hester, J. J., Raymond, J. C., & Petre, R. 1995, *ApJ*, 444, 787
 Hester, J. J. 1987, *ApJ*, 314, 187
 Hester, J. J., & Cox, D. P. 1985, *ApJ*, 300, 675
 Hester, J. J., Raymond, J. C., & Blair, W. P. 1994, *ApJ*, 420, 721
 Holtzman, J. A., Burrows, C. J., Casertano, S., Hester, J. J., Trauger, J. T., Watson, A. M. & Worthey, G. 1995, *PASP*, 107, 1065
 HST Data Handbook, Vol. 1, Ed. M. Voit 1998, (STScI: Baltimore)
 Innes, D. E. 1992, *A&A*, 256, 660
 Klein, R. I., McKee, C. F., & Colella, P. 1994, *ApJ*, 420, 213
 Ku, W. H.-M., Kahn, S. M., Pisarski, R., & Long, K. S. 1984, *ApJ*, 278, 615
 Levenson, N. A., Graham, J. R., Hester, J. J., & Petre, R. 1996, *ApJ*, 468, 323
 Levenson, N. A., Graham, J. R., Keller, L. D., & Richter, M. J. 1998, *ApJS*, 118, 541
 Levenson, N. A., Graham, J. R., & Snowden, S. L. 1999, *ApJ*, 526, 874

- McKee, C. F., & Cowie, L. L. 1975, ApJ, 195, 715
Parker, R. A. R. 1967, ApJ, 149, 363
Raymond, J. C. 1979, ApJS, 39, 1
Raymond, J. C. 1991, PASP, 103, 781
Raymond, J. C., Hester, J. J., Cox, D., Blair, W. P., Fesen, R. A.,
& Gull, T. R. 1988, ApJ, 324, 869
Sankrit, R., Blair, W. P., Raymond, J. C., & Long, K. S. 2000, AJ,
120, 1925
Spitzer, L. 1982, ApJ, 262, 315
Vancura, O., Raymond, J. C., Dwek, E., Blair, W. P., Long, K. S.,
& Foster, S. 1994, ApJ, 431, 188